Applied Physics A (2023) 129:517
https://doi.org/10.1007/s00339-023-06752-5

Applied Physics A
Materials Science & Processing

Aqueous synthesis of CdSeTe-alloyed quantum dots, fabrication of CdSeTe, CdS and CdSe QDs-sensitized solar cells and optimization of the sensitizing, light scattering and passivating layers

M. Marandi[1] · N. Shahidi[2] · S. Hossein Abadi[1]

Received: 25 February 2023 / Accepted: 31 May 2023 / Published online: 28 June 2023

Abstract
In this research, quantum dot-sensitized solar cells (QDSCs) with multilayer photoelectrodes, i.e., the TiO_2 nanocrystals/CdSeTe/CdS/CdSe/ZnS, were fabricated and investigated. The CdSeTe nanocrystals (NCs) were easily synthesized in aqueous solution and deposited on nanocrystalline TiO_2 scaffold through drop-casting method. The other sensitizing/passivizing films were also prepared by successive ionic layer adsorption and reaction (SILAR) and chemical bath deposition (CBD) methods. It was shown that QDSC with TiO_2 nanocrystals/CdSeTe/CdS/ZnS photoanode demonstrated an energy conversion efficiency of 2.95%. This efficiency was enhanced about 30% through the addition and optimization of a CdSe QDs film in the photoelectrode. The CdSe-sensitizing film was effectively deposited in just 9 min and ZnS was applied as the normal passivating film. In the next stage, TiO_2 hollow spheres (HSs) were prepared with desired dimension via a template scarifying approach to enhance the light travelling path inside the photoelectrode and increase the light harvesting efficiency. The mentioned point resulted in 12% enhancement compared to the HSs-free QDSC. The last improvement was finally performed by optimization of the ZnS passivating layer and showed a 30% improvement in PCE of the final QDSC in comparison with HSs-free CdSeTe/CdS/CdSe-sensitized solar cell. The pioneer cell was compared with the CdSe and HSs-free reference cell which demonstrated a considerable 68% enhancement in photovoltaic performance.

Keywords CdSeTe NCs · Aqueous synthesis · Multilayer photoelectrode · CdSe QDs · Light scattering layer

1 Introduction

Quantum dot-sensitized solar cells (QDSCs) have been under extensive researches in two recent decades [1–4]. These photovoltaic devices are one of the most promising kinds of solar cells as they are using the novel advantages of semiconductor quantum dots (QDs) [5–9]. The size tunable bandgap energy [10, 11], multiple exciton generation [12, 13], high absorption coefficient [14] and absorbance in wide ranges of wavelengths [15] are the most important characteristics of the sensitizing NCs [15–17] In the photoanode of QDSCs, the wide bandgap mesoporous scaffold creates a large surface area for deposition of different layers of light absorbing QDs [17] These layers could efficiently absorb the different regions of the incident solar spectrum [18]. Some passivating layers are also over-deposited on the photo electrode to reduce the inappropriate charge carrier's recombination [19, 20].

Several researches have been carried out on different components of QDSCs to improve the photovoltaic (PV) performance. The utilization of various nanostructured scaffolds [6, 21–25] co-sensitization with several layers of different semiconductor quantum dots [18, 26–29] application of effective recombination passivizing layers [18, 19, 30] different liquid ionic or gel/solid electrolytes and various compositions/structures of counter electrodes have been studied and investigated [31–36].

Co-sensitization is one of the main ideas for enhancement of power conversion efficiency (PCE) of QDSCs [37, 38]. Different photoanode structures such as TiO_2 mesoporous layer/CdS/ZnS [39], TiO_2 mesoporous layer/CdS/CdSe/ZnS

✉ M. Marandi
m-marandi@araku.ac.ir

[1] Physics Department, Faculty of Science, Arak University, Arak 38156, Iran

[2] Farzanegan High School, National Organization for Development of Exceptional Talents (Sampad-NODET), Arak 3815899975, Iran

[40], TiO_2 mesoporous layer/PbS/CdS/CdSe/ZnS [41] and TiO_2 mesoporous layer/CdSeTe/ZnS [42] have been fabricated and investigated. The CdS, CdSe and CdSeTe NCs films could efficiently absorb specific parts of solar spectrum [43, 44]. That is while the photo generated charge carries in different layers can be well-transferred in the cell without potential barriers and in right directions [45, 46] The corresponding PCEs for the above mentioned photoanodes are in the range of 0.5–2.3% [39, 40], 2.5–7% [40, 47], 3–3.5% [41] and 4–5% [42], respectively.

CdSeTe NCs have been synthesized through high temperature expensive organometallic approach and individually applied in QDSCs [48–51]. The corresponding efficiencies were quite high due to the wide range of light absorption even in NIR region [52–56]. Meanwhile, the aqueous synthesis of alloyed CdSeTe NCs is still attractive owing to the simple synthesizing method and cheaper nontoxic materials [52, 57–59]. A few works have been done in this area especially with multi-layer photoelectrodes to check the effect of co-sensitization. The reported efficiencies for the CdSeS and CdSeTe photoanode structures where in the range of 3–6.3% [47, 60] and 4–7.5% [42, 56, 61].

In this work a novel multi-layer photoanode of QDSCs with TiO_2 NCs/HSs/CdSeTe/CdS/CdSe/ZnS structure was fabricated and studied. CdSeTe-alloyed NCs were ex-synthesized in aqueous solution through a facile chemical precipitation/refluxing method. Then, they were drop-casted and another CdS nanocrystalline film was over deposited through a successive ionic layer adsorption and reaction (SILAR) approach. The third CdSe-sensitizing film was also formed on the underlying layers by a fast effective chemical bath deposition (CBD) method. Finally a ZnS passivating layer was deposited and QDSCs were completed using polysulfide electrolyte and CuS counter electrode. The CBD time was altered for optimization of CdSe-sensitizing film and efficiency was considerably increased compared to the CdSe-free similar QDSC. The TiO_2 hallow spheres (HSs) were finally applied to make a double layer mesoporous scaffold with higher level of light scattering/absorption. The utilization of TiO_2 HSs layer and optimization of passivating film were carried out and demonstrated a 68% increase in PCE compared to that of the CdS and HSs-free QDSC.

2 Experimental

2.1 Synthesis of TiO_2 nanoparticles

TiO_2 nanoparticles were synthesized through a hydrothermal method as follows in the first step, 0.014 ml of acetic acid and the same mole of titanium tetraisoproxide (TTIP) were mixed and stirred for about 15 min. Then, 19.6 ml of DI water was added to this solution for the hydrolysis process and stirred for more than 1 h [6, 40]. The solution was quite white and there was precipitations demonstrating the existence of TiO_2 agglomerates which should be re-dispersed. This was carried out by injection of 0.26 ml of HNO_3 and refluxing the solution at 80 °C for 75 min. The final pale blue TiO_2 sol was transferred to a teflon-lined stainless-steel autoclave and heated at 230 °C for 12 h to fulfill the hydrothermal growth. Afterward, the TiO_2 precipitate was centrifuged and washed with ethanol for several times to remove the extra water for the TiO_2 paste preparation, specific amounts of ethyl cellulose as the viscosity modifying agent and terpineol ($C_{10}H_{18}O$) were dissolved in absolute ethanol. Then, they were added to the sol of TiO_2 nanoparticles in ethanol. Ultrasonic process was carried out with an ultrasonic probe (400 w) for three 20 min steps and the solution was stirred for one night. Finally, a viscous TiO_2 paste was obtained through the vacuum evaporation of ethanol solvent which was composed of 18 wt% TiO_2 NC_S, 73 wt% terpineol and 9 wt% of ethyl cellulose. Doctor blading method was applied for deposition the fresh TiO_2 paste on the glass–FTO substrates with a sheet with 15 Ω/cm^2. The prepared layers were annealed in 4 successive steps, i.e., at 325, 375, 450 and 500 °C for 50, 5, 15, and 15 min. This was carried out for the polymer elimination and obtaining better crystalline quality and sintering of the TiO_2 nanocrystals in mesoporous layer. The final thickness of TiO_2 layer was set to be around 10 µm and named as $H1_2$ as two layers of scotch tape was used as the spacer and layer was deposited in one time of doctor blading. If one layer of spacer tape was utilized, the thickness of TiO_2 film was around 5 µm and the layer was specified as H1.

2.2 Preparation of TiO_2 hollow spheres

TiO_2 hollow spheres were also synthesized by another hydrothermal process as was mentioned in our previous articles [40, 62]. For this goal, 25 ml of 1 M aqueous solution of glucose was prepared and transferred to a teflon-lined stainless-steel autoclave and heated at 180 °C for 12 h. Then, the final solution was centrifuged and washed with ethanol and deionized water for several times. In the last step, the carbon precipitate was dried at 70 °C for 5 h to form a fine structured dried powder. For the TiO_2 shells formation on the surface of carbon spheres, 0.4 g of carbon spheres powder was dissolved in 40 ml of ethanol solution and sonicated for 40 min. Then, 0.004 mol (0.12 ml) of TTIP was added to the previous solution and stirred at room temperature for 24 h for completion of the liquid phase deposition (LPD) process. The resulting solution was centrifuged and washed with ethanol and DI water for several times. Then, the core–shell carbon spheres/TiO_2 precipitate was annealed at 40 °C for 12 h to be dried. Subsequently, the carbon cores were eliminated through a calcination at 450 °C for 2 h and

TiO_2 hollow spheres were remained. The paste preparation process with TiO_2 HSs was composed of the same stages as the TiO_2 NCs [6]. Briefly, 0.24 g of TiO_2 HSs, 0.13 g of ethyl cellulose, 6.5 g of terpineol were dissolved in 40 ml ethanol and stirred for several hours to form a totally dispersed homogenic solution. Then, it was vacuum evaporated to make a paste composed of 18 wt% TiO_2 NC, 73 wt% terpineol and 9 wt% ethyl cellulose. TiO_2 HSs were deposited on the surface of FTO/H1 substrates with H1 TiO_2 nanocrystalline layer with a thickness around 5 µm. The final H1/HSs bilayer scaffold was applied in the photoelectrode of the fabricated QDSCs after an annealing process the same as what was carried out for the nanocrystalline TiO_2 film.

2.3 Preparation of the CdSeTe quantum dots

A modified chemical precipitation method was applied for the synthesis of CdSeTe NCs in aqueous solution. Briefly, for the synthesis of NaHTe Te precursor solution, 10 ml of DI water and 1.25 mmol of sodium borohydride were transferred into a three-neck flask and mixed for about 15 min under the argon flow. Afterward, 0.5 mmol of tellurium powder was added and solution was vigorously stirred for 2 h. The color of solution was turned from the dark-violet to a transparent light-pink during the stirring. In parallel, the NaHSe solution was prepared through a similar procedure using Se powder and the solution color changed from black to colorless after 1 h of stirring. In another aqueous solution, 0.72 mmol of the thioglycolic acid (TGA) capping material and 0.5 mmol of $CdCl_2$ were dissolved in 100 ml of DI water and stirred. The corresponding pH was adjusted on 11.0 by addition of a few drops of 1 M, NaOH solution. The oxygen purging was carried out using Ar flow and solution was intensely stirred in a three-neck flask under for 30 min. The vessel was heated at 100 °C in an oil bath for 10 min for the hot injection. Then, $1-X$ ml of the light-pink NaHTe, ($X=0.6$) and X ml of the colorless NaHSe solutions were simultaneously injected to the Cd-TGA complex solution and refluxing was done for 7 h.

2.4 Deposition of CdSeTe, CdS and CdSe QDs layers and cells fabrication

The $H1_2$ TiO_2 mesoporous scaffolds were sensitized with alloyed CdSeTe–CdS NCs, CdS and CdSe QDs layers. For this purpose, the dispersed CdSeTe NCs in NaOH solution were deposited on TiO_2 nanocrystalline substrate via a drop-casting method. The deposition time was 2 h for the appropriate formation of the CdSeTe NCs film. The second sensitization was carried out by deposition of the CdS QDs layer through the conventional SILAR process. The TiO_2 NCs/CdSeTe double layers were immersed in a 0.1 M solution of $Cd(CH_3COO)_2$ in methanol for 1 min and rinsed with methanol. Then, they were dipped in 0.1 mol solution of $Na_2S{\cdot}9H_2O$ in methanol and water (50:50, V/V) for another 1 min and washed again. The SILAR deposition was carried out for 4 successive cycles and well surface coverage was achieved.

The last sensitizing film was CdSe which was deposited through a chemical bath deposition (CBD) technique. Here, an Na_2SeSO_3 aqueous solution was first prepared by refluxing a 0.158 g of Se, 2.777 g Na_2SO_3 and 20 ml deionized water at 80 ◦C for 4 h and filtered. Then, 2.5 ml of this solution was added to 22.5 ml of DI water and 0.014 g $Cd(CH_3COO)_2{\cdot}2H_2O$ was perfectly dissolved in final solution. A little amount of the solution was taken and 0.02 g Ammonium hydroxide (NH_4OH) was dissolved in it and returned to the reaction vessel. The FTO/CdSeTe/CdS photoelectrodes were put in the as prepared solution (chemical bath) at 95 °C and CBD time was changed between 0 and 15 min. The photoanodes were named as $H1_2$/CdSeTe/CdS/CdSe(X min) and H1/HSs/CdSeTe/CdS/CdSe(X min) in the article, where X demonstrates the CBD time. At the final stage, the photoelectrodes were coated with ZnS passivating films. The ZnS layer was deposited via 1–2 cycles of a SILAR process using a 0.1 M $Zn(CH3COO)_2$ and 0.1 M $Na_2S{\cdot}9H_2O$ solutions in water and the dipping times were both 2 min.

To assemble the QDSCs, the prepared $H1_2$/CdSeTe/CdS/CdSe/ZnS, H1/HSs/CdSeTe/CdS/CdSe/ZnS photoanodes were sandwiched with a copper sulfide (CuS) counter electrode. The CuS was also prepared by SILAR deposition method using a 0.5 M solution of $Cu(NO_3)_2$ in ethanol and 0.5 M $Na_2S{\cdot}9H_2O$ solution in ethanol/water (50:50, V/V). The polysulfide redox liquid electrolyte was also prepared using 1 M Na_2S, 1 M S (99.0%) and 2 M KCl (99.5%) precursor which were dissolved in methanol/water solution (7/3, V/V) in a three-neck flask and stirred for 30 min under the Ar gas flow. Then, the other fabrication steps of the QDSCs including the electrolyte injection into the space between the photoanode and the CE and cell sealing were performed.

2.5 Characterizations

Field emission electron microscopy (FESEM) and EDX measurements were performed using a MIRA3 TESCAN XMU system. The X-ray diffraction patterns were recorded by a Philips Xpert-pro equipment with a Cr Kα ($\lambda=2.29$ Å) X-ray radiation. Optical spectroscopies were carried out using a Mecasys Optizen POP UV–Vis spectrophotometer. The recording process of the photoluminescence spectra of alloyed NCs was done through an excitation with 360 nm UV light and sending the emission into an avantes 2048L spectrophotometer by optical fibers. Diffuse reflection spectra were measured using a deuterium–halogen light source and the reflection was collected through an integrating sphere

and transferred to an Avantes 2048L spectrophotometer. The measurements of the current density–voltage characteristics were performed under AM 1.5, 100 mW/cm^2 simulated sun light irradiation using a Sharif solar system. The incident photon to current conversion efficiencies (IPCE) were also recorded by a Sharif solar IPCE equipment.

3 Results and discussion

CdSeTe QDs were synthesized in aqueous solution since lower toxicity of materials, inexpensive and simpler method and also the safe experimental conditions [42]. According to experimental section, only three CdSeTe samples were applied in this research, since the last sample prepared at 11 h of reflux time was agglomerated and deformed. Figure 1a demonstrates the transmission spectra of CdSeTe NCs prepared in the reflux time of 1, 7 and 10 h. According to the results, the absorption edge is of NCs is shifted to the longer wavelengths because of the size enhancement and reduction of the bandgap energy. It could be observed that the absorption edge is located around 535 nm for the CdSeTe(1 h) NPs. This is red-shifted to 575 and 595 nm for the CdSeTe(7 h) and CdSeTe(10 h), respectively. The mentioned shift is corresponded to a bandgap energy change from 2.31 to 2.08 eV for the synthesized samples. Here, the turning point of the transmission spectra in absorption region is selected as the bandgap energy of the samples. The photoluminescence measurement was also carried out and the results are shown in Fig. 1b. It is seen that the PL peak position is altered from 534 to 589 nm by prolonging the reflux time from 1 to 10 h. If we change the PL peak wavelengths to the energy the extracted numbers are 2.31, 2.12 and 2.10 eV which are close to the bandgap energies achieved from the transmission spectra. The corresponding PL quantum yields of the NCs were also calculated in comparison with uranine reference material and revealed the values of 7%, 16% and 11% as the reflux time is increased. This demonstrates the higher PLQY for the sample prepared in 7 h of the heating and better crystalline quality.

As mentioned earlier, the alloyed NCs were named as CdSeTe(X h); ($X = 1, 7, 10$) in the experiments. The typical X-ray diffraction pattern of the CdSeTe(7 h) nanoparticles was recorded and indicated in Fig. 1c. It is obvious that there are three clear and widened peaks located at 2Θ angles of 37.19°, 62.71° and 75.12°. These peaks belong to the (002), (110) and (112) crystalline planes of hexagonal phase of CdSeTe material (JCPDS File No 00-041-1325). Finally the samples were placed under the UV light ($\lambda = 360$ nm) and emission images are shown in Fig. 1d to create a better sense about the color and emission color of the particles.

CdSeTe(7 h) quantum dots were selected as a result of their appropriate bandgap energy and mainly the higher PL quantum yield. This could show the better crystalline quality

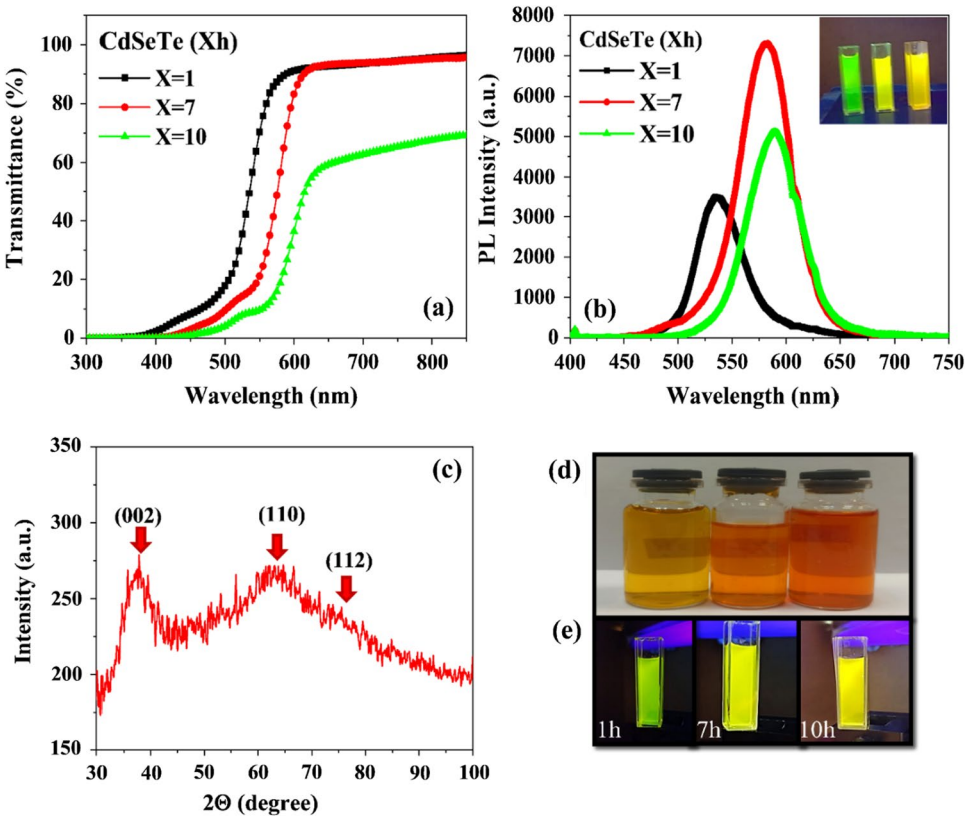

Fig. 1 Optical transmission (**a**) and photoluminescence spectra (**b**) of the CdSeTe NCs during the reflux time. X-ray diffraction pattern of the typical CdSeTe(7 h) (**c**) and real images of the QDs solutions (**d**) and their emission under UV light excitation (**e**)

and lower density of trap states which could lower the undesirable photogenerated electron–hole pairs and create higher current density in fabricated QDSCs. Consequently these particles were deposited on TiO_2 mesoporous scaffold, i.e., the electron transport layer as the first sensitizing layer of the photoelectrodes. Then, they were covered with two extra sensitizing films of CdS and CdSe QDs for more improved light absorption. Meanwhile, the CdSe QDs layer was deposited through a fast CBD technique and deposition time was altered in the range of 0–15 min in the experiments. In the first stage TiO_2, nanocrystalline scaffold was utilized which was formed of hydrothermally grown TiO_2 NPs deposited through doctor blade method on glass FTO substrate. This was named as $H1_2$ as was fully explained in experimental section. The corresponding SEM images of the $H1_2$ TiO_2 layer is shown in Fig. 2a, b in different magnifications. It is seen that the particles are round shape and nearly uniform in size. Besides, the formed mesoporous layer is crack-free as it is clearly shown in larger windows, i.e., in Fig. 2a. The size distribution histogram of the composing particles are also extracted and shown in the inset of Fig. 2b. It could be observed that the dominant size is about 20 nm, while there are other sizes in the range of 15–20 nm.

As was explained the co-sensitized $H1_2$/CdSeTe/CdS(4c)/CdSe(Y min), $Y=0$, 6, 9, 12, 15, photoelectrodes were fabricated and corresponding transmission spectra are shown in Fig. 3. The transmission spectra of the $H1_2$ TiO_2 sublayer and $H1_2$/CdS-sensitized film is also shown for comparison. It could be seen that $H1_2$ TiO_2 layer is quite transparent with a transparency about 80% in longer wavelengths. The optical absorption edge is also positioned around 500 nm which is corresponded to the bandgap energy of TiO_2. The absorption edge is red-shifted to about 500 nm after deposition of CdS

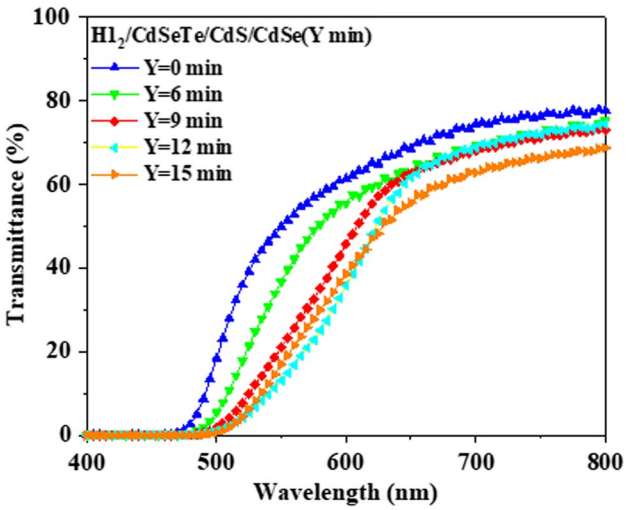

Fig. 2 Optical transmission spectra of the $H1_2$/CdSeTe/CdS(4c)/CdSe(Y min), $Y=0$, 6, 9, 12, 15, photoelectrodes

film due to the band to band light absorption by this sensitizing film. The transmission spectrum shows a decrease in intensity for the wavelength range of 550–650 nm for the $H1_2$/CdSeTe/CdS(4c) photoanode. This is due to the light absorption by CdSeTe layer and also the corresponding low thickness achieved through drop casting approach. Meanwhile, for the $H1_2$/CdSeTe/CdS(4c)/CdSe(Y min), $Y=0$–15, The absorption edge of the spectrum is obviously moved toward the longer wavelengths in the range of 550–600 nm. The shift is enhanced as the CBD deposition time of CdSe layer is increased. This is attributed to the larger size of CdSe QDs in the layer and their lower bandgap energy. Besides, the lower transmittance in long wavelengths is created by increased light scattering of the CdSe film as the roughness is intensified for thicker CdSe layers.

The final ZnS passivating film was also deposited on the photoanodes surface trough one SILAR cycle, 2 min, as was explained earlier. The corresponding J–V characteristics of the $H1_2$/CdSeTe(7 h)/CdS(4c)/CdSe(Y min)/ZnS(1c-2 min), ($Y=0$, 6, 9, 12, 15), photoanodes were recorded and demonstrated in Fig. 4a. The related schematic of flat band energy diagram of the cells is also depicted and shown in Fig. 4b for the clearance of the electrons and holes transfer between the layers. According to the photovoltaic parameters which are extracted and shown in Table 1, the reference cell with $H1_2$/CdSeTe(7 h)/CdS(4c)/ZnS(1c-2 min) photoelectrode represents a $J_{sc}=7.15$ mA/cm^2, $V_{oc}=596$ mV, FF = 0.68 and PCE = 2.95%. The J_{sc}, V_{oc} and PCE are increased by deposition of CdSe layer and enhanced for longer CBD deposition time. Finally, the photovoltaic parameters reach to their maximum value of $J_{sc}=12.55$ mA/cm^2, $V_{oc}=647$ mV and $\eta=3.79\%$ for the co-sensitized cell with $H1_2$/CdSeTe(7 h)/CdS/CdSe(9 min)/ZnS photoelectrode. This is due to the co-adsorption of the incident light by CdSe(9 min) QDs layer with high crystalline quality and well-transport/transfer of charge carriers inside the cell. Meanwhile, the efficiency is decreased for the QDSCs with $H1_2$/CdSeTe(7 h)/CdS/CdSe(Y min)/ZnS, $Y=12$–15, photoanodes. This is due to the higher thickness of the CdSe-sensitizing layer and the higher resistance together with preventing the electrolyte from the well penetration into the photoanode and other sensitizing films.

To improve the photovoltaic performance of the fabricated QDSCs, TiO_2 hollow spheres were utilized in the photoelectrodes. As mentioned in experimental section, TiO_2 HSs were prepared and deposited on the TiO_2 NCs sublayer as the light scattering film. The top view SEM images of the H1 TiO_2 mesoporous layer is shown in Fig. 2a, b. Here, the SEM images of H1/HSs double-layer scaffold are demonstrated in Fig. 5a, b. It is nicely represented that the TiO_2 HSs are well-formed and their shape are saved in the layer. They are nearly spherical and perforated in some cases due to the exhaust of CO_2 gas in the carbon templates burning

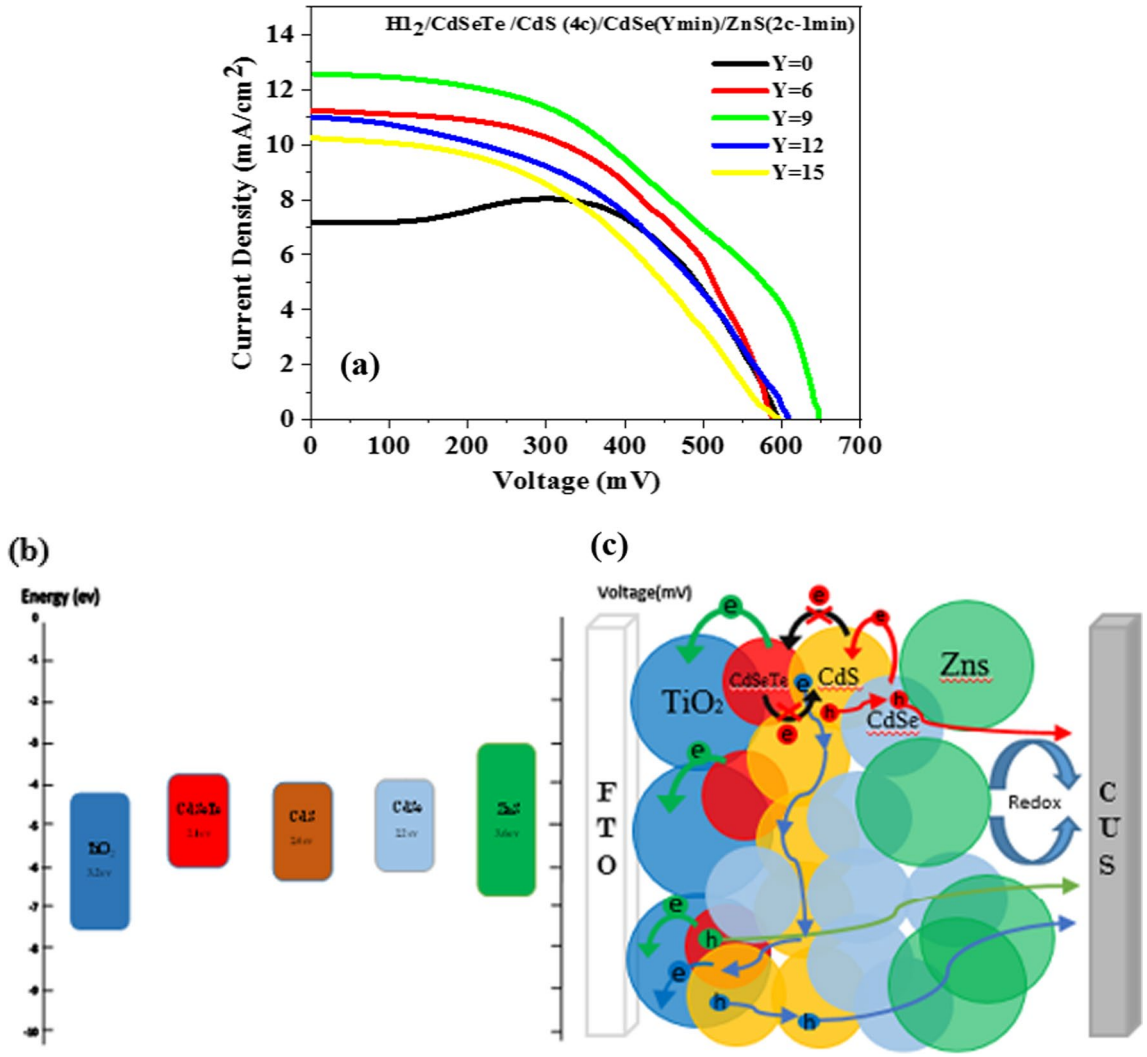

Fig. 3 *J–V* characteristics of the fabricated QDSCs with H1$_2$/CdSeTe/CdS(4c)/CdSe(*Y* min)/ZnS(1c-2 min); *Y* = 0, 6, 9, 12, 15 photoanodes (**a**). Flat band energy diagram of the photoelectrode (**b**) and schematic of a fabricated cell (**c**)

stage. The external diameter distribution histogram is also extracted from the several images and shown in the inset of Fig. 5a. According to result, the dominant external dimeter is about 550 nm which is quite appropriate for generation of light scattering in visual region of solar incident light. The top view SEM images of the CdSeTe QDs-sensitized photoanode are demonstrated in Fig. 5c, d. It is obvious that a little change in the surface morphology of the H1/HSs scaffold is created. This is due to the low thickness of CdSeTe-alloyed QDs and deposition by drop casting method. Meanwhile, the surfaces of the H1/HSs/CdSeTe/CdS and H1/HSs/CdSeTe/CdS/CdSe(9 min) photoelectrodes are clearly altered and small particles/agglomerations are formed on the HSs film. This is represented in the SEM images of Fig. 5e, f. The reason can be attributed to the deposition of CdS and CdSe QDs layer through SILAR and CBD methods. The density of these sensitizing particles is also enhanced for the CdSeTe/CdS/CdSe(9 min)-sensitized photoanode owing to the double layer sensitization. The cross-sectional SEM image of the H1/HSs/CdSeTe/CdS/CdSe(9 min) photoanode is shown in Fig. 5g. As shown in the figure, the H1 TiO_2 NCs layer and HSs overlayer are quite recognizable and the corresponding thicknesses are measured about 5 and 12 µm, respectively. Finally, the front and backside real images of the H1 and H1/HSs scaffold and H1/HSs/CdSeTe, H1/HSs/CdSeTe/CdS and H1/HSs/CdSeTe/CdS/CdSe photoanodes are delivered in Fig. 5h.

The energy dispersive X-ray spectroscopy (EDX) was also carried out for the H1/HSs/CdSeTe/CdS/CdSe/ZnS(1c-2 min) photoelectrode to clarify the composing elements. As the results are shown in Fig. 5a, there are several peaks related to the Ti, O, S, Se, Te, Zn and Cd elements in the spectrum. The atomic percents of included elements in the photoanode are also extracted and demonstrated in the

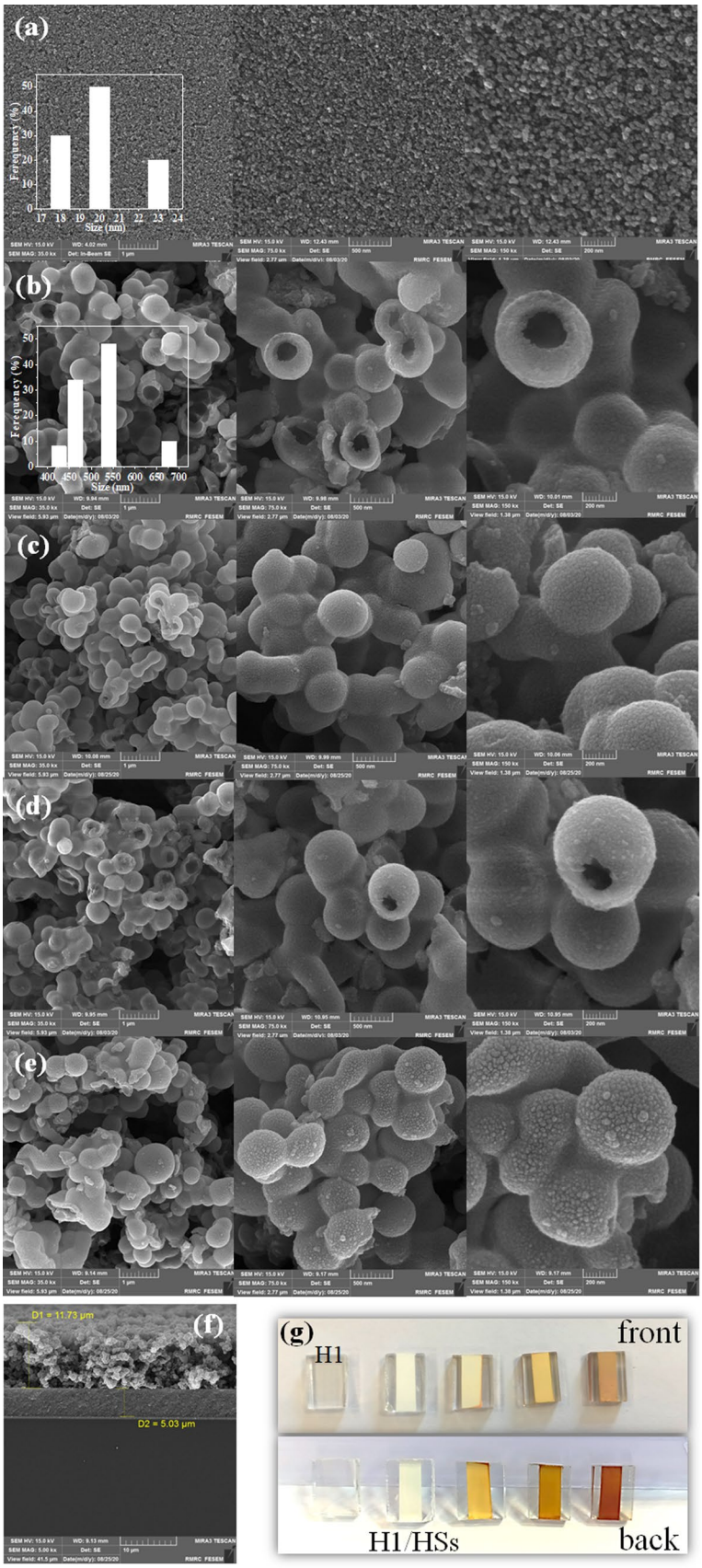

Fig. 4 Top-view FESEM images of the H1 nanocrystalline film (**a**), H1/HSs scaffold (**b**) and H1/HSs/CdSeTe (**c**), H1/HSs/CdSeTe/CdS (**d**) H1/HSs/CdSeTe/CdS/CdSe (**e**)-sensitized TiO_2 layers in different magnifications. The corresponding size distribution histograms of the TiO_2 nanoparticles and hollow spheres are shown in the inset of the figures (**a**, **b**). Cross-sectional SEM image of the TiO_2 H1/HSs scaffold (**f**) and front and back side images of the sub-layer and sensitized photoelectrodes in different sensitizing stages (**g**)

Table 1 Photovoltaic parameters of the QDSCs with $H1_2$/CdSeTe/CdS/CdSe(*Y* min)/ZnS(1c-2 min); *Y* = 0, 9, 6, 12, 15 photoelectrodes

Photoanode	J_{sc} (mA/cm^2)	V_{oc} (mV)	FF	η (%)
$H1_2$/CdSeTe/CdS/CdSe(0 min)/ZnS	7.15	596	0.68	2.95
$H1_2$/CdSeTe/CdS/CdSe(6 min)/ZnS	11.25	590	0.52	3.45
$H1_2$/CdSeTe/CdS/CdSe(9 min)/ZnS	12.56	647	0.47	3.80
$H1_2$/CdSeTe/CdS/CdSe(12 min)/ZnS	11	608	0.45	3
$H1_2$/CdSeTe/CdS/CdSe(15 min)/ZnS	10.25	595	0.44	2.7

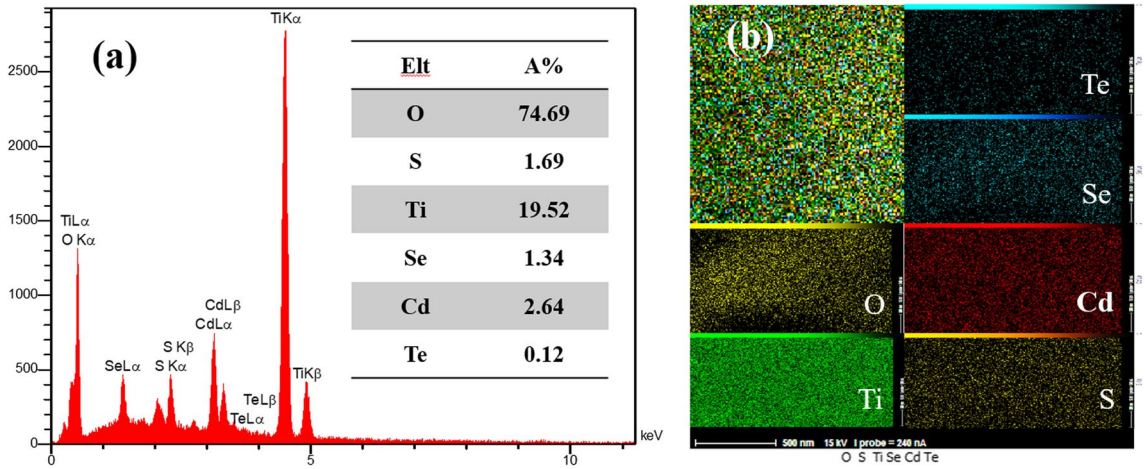

Fig. 5 EDX spectrum of the H1/HSs/CdSeTe/CdS/CdSe photoelectrode (**a**) and the results of MAP analysis (**b**) for including Cd, Te, Se, S, Ti and O elements. The table of atomic percent of all detected elements is shown in the inset of a view

inset of the figure. According to results, the atomic ratio of (S + Te + Se)/Cd is measured about 0.83 which is close to one and reveals the formation of the CdSeTe, CdS and CdSe-sensitizing films. The MAP analysis is additionally performed and related images are represented in Fig. 5b. What is clear in the result is the uniform distribution of the composing elements in the photoelectrode which plays a key role in the PV performance of the fabricated QDSCs.

The X-ray diffraction patterns of the H1 and H1/HSs scaffolds and H1/HSs/CdSeTe, H1/HSs/CdSeTe/CdS and H1/HSs/CdSeTe/CdS/CdSe-sensitized TiO_2 sublayers are recorded and shown in Fig. 6. As shown in Fig. 6a, the H1 nanocrystalline sublayer demonstrates some obvious peaks located at 2θ angles of 37.95°, 57.60°, 74.35°, 84.55° and 86.60°. These peaks are related to the (101), (004), (200), (105) and (211) crystalline planes of the anatase phase TiO_2 based on the JCPDS file No 01-086-1157. The crystallite size of TiO_2 composing nanoparticles could be calculated using the FWHM of the (101) peak and Scherrer formula [63, 64]. This size is achieved about 20 nm which is in agreement with the real particles size which was extracted from the corresponding SEM images. The XRD spectrum of the H1/HSs double layer scaffold is demonstrated in Fig. 6b and represents similar peaks as the H1 nanocrystalline TiO_2 film. This shows that the HSs have the same anatase crystalline

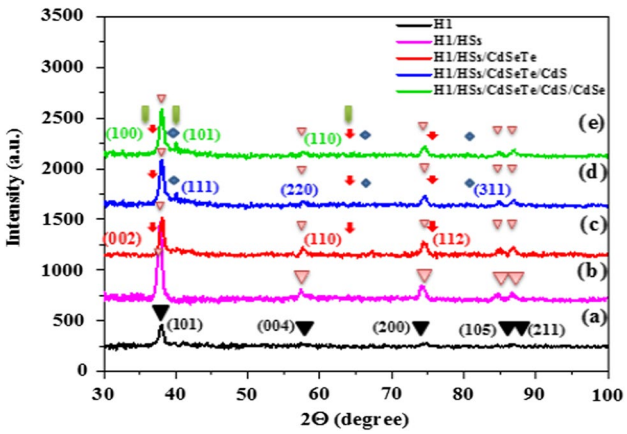

Fig. 6 X-ray diffraction patterns of the mesoporous H1 (**a**) and H1/HSs (**b**), H1/HSs/CdSeTe (**c**), H1/HSs/CdSeTe/CdS(4c) (**d**) and H1/HSs/CdSeTe/CdS/CdSe(9 min) photoelectrodes (**e**)

phase like the hydrothermally grown TiO_2 NPs. For the light-sensitized H1/HSs/CdSeTe, H1/HSs/CdSeTe/CdS and H1/HSs/CdSeTe/CdS/CdSe photoanodes, the standard XRD peak positions and corresponding crystalline planes of the hexagonal crystal phase of CdSeTe, cubic phase of CdS and hexagonal Phase of CdSe are shown on the spectra using the JCPDS files No. 00-041-1325, 00-001-0647 and

00-002-0330, respectively. It could be seen that the CdS-related peaks are slightly recognizable, while the others are quite unclear due to the comparative low thickness of sensitizing films to the TiO_2 sublayer.

Figure 7a displays the transmission spectra of the H1 and H1/HSs scaffolds and also the sensitized H1/HSs/CdSeTe, H1/HSs//CdSeTe/CdS and H1/HSs//CdSeTe/CdS/CdSe photoelectrodes. Again it is clear that the H1 nanocrystalline TiO_2 layer is well-transparent and the oscillations in long wavelengths reveal the smooth surface and light interference consequences. Meanwhile, the value of transmission for the double layer H1/HSs and other sensitized photoelectrodes is nearly zero owing to the high intensity of light scattering created by TiO_2 HSs film. This can make the photoanodes as some quite opaque multilayers and the white appearance of the H1/HSs scaffold could justify the mentioned point. The corresponding diffuse reflectances of the photoanodes are demonstrated in Fig. 7b. It is observed that the TiO_2 nanocrystalline film shows a low reflectance, i.e., lower than 10% due to its high level of transparency. Meanwhile, the reflectance is increased to around 80% for the H1/HSs double layer scaffold which confirm the high level of light scattering. The absorption edge is also about 380 nm and is related to the bandgap energy of TiO_2, i.e., the 3.2 eV. According to the results there is an absorption in the wavelengths below 600 nm for the H1/HSs/CdSeTe-sensitized photoanode which is attributed to the CdSeTe NPs layer. This is in correspondence with the absorption of these synthesized particles, as shown in Fig. 1a, b. The deposition of CdS-sensitizing film created a higher absorption in the wavelengths about 500 nm due to the higher thickness which is deposited through the SILAR method. Finally, for the H1/CdSeTe/CdS/CdSe photoanode the absorption edge is quite red-shifted to the range of 600–650 nm which shows the effective deposition of CdSe-sensitizing film with appropriate thickness by CBD approach.

Figure 8a represents the J–V characteristics of the fabricated QDSCs with $H1_2$/CdSeTe/CdS/CdSe/ZnS(1c-2 min) and H1/HSs/CdSeTe/CdS/CdSe/ZnS(*N*c-2 min), $N = 1$, 2, photoanodes. Here, N shows the number of deposition cycles for the ZnS passivating layer with dipping time of 2 min. The corresponding photovoltaic parameters are also extracted and shown in Table 2.

As it is recorded, the reference cell with $H1_2$/CdSeTe/CdS/CdSe/ZnS(1c-2 min) photoanode demonstrates a $J_{sc} = 12.55$ mA/cm^2, $V_{oc} = 647$ mV, FF = 0.47 and PCE of 3.8%. Meanwhile, The J_{sc} is increased to 13.75 mA/cm^2 and the FF and η are enhanced to 0.52% and 4.25% for the co-sensitized cell with H1/HSs/CdSeTe/CdS/CdSe/ZnS(1c-2 min) photoanode. It is necessary to mention that the thickness of nanocrystalline TiO_2 layer is about 5.0 µm and half of the thickness of NCs sublayer in the reference cell. As the quantum dots adsorption on the photoanode surface is mainly done by nanocrystalline layer and HSs have a slight role. It obvious that the observed enhancement is due to the HSs light scattering which increase the light traveling path/light absorption in corresponding photoelectrode. In addition, for the similar cell with two cycles of ZnS deposition cycles, the photovoltaic parameters are improved to $J_{sc} = 15.1$ mA/cm^2, $V_{oc} = 575$ mV, FF = 0.57 and PCE = 4.92%. This shows that fabricated QDSC with H1/HSs/CdSeTe/CdS/CdSe/ZnS(2c-2 min) photoanode reveals the maximum power conversion efficiency and an enhancement about 30% compared to the reference cell. The reason could be attributed to the better surface passivation/lower density of char carriers trap states in the photoanode/

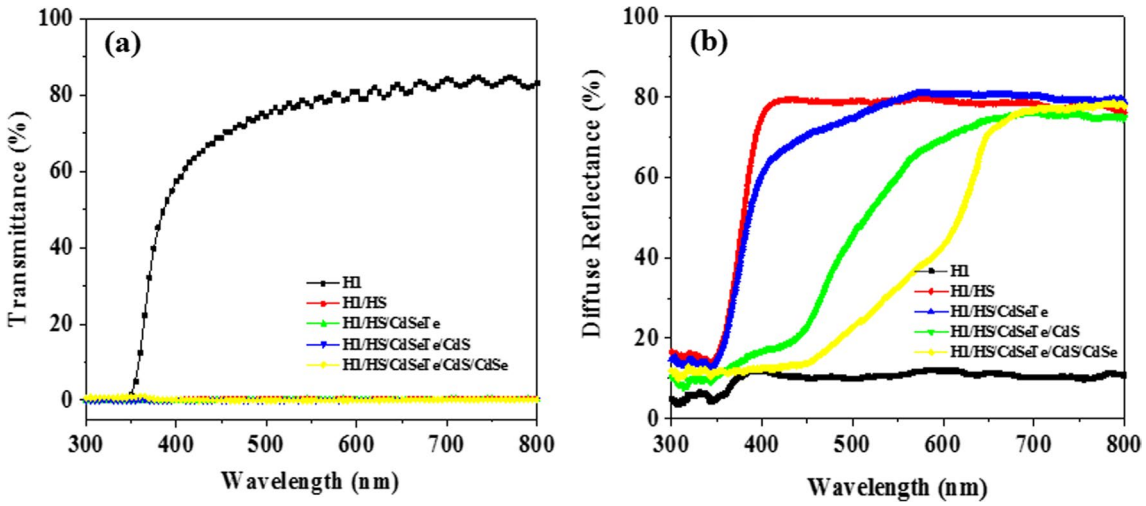

Fig. 7 Optical transmission (**a**) and diffuse reflectance spectra (**b**) of the H1 and H1/HSs TiO_2 scaffolds and H1/HSs/CdSeTe, H1/HSs/CdSeTe/CdS(4c) and H1/HSs/CdSeTe/CdS/CdSe(9 min) photoelectrodes

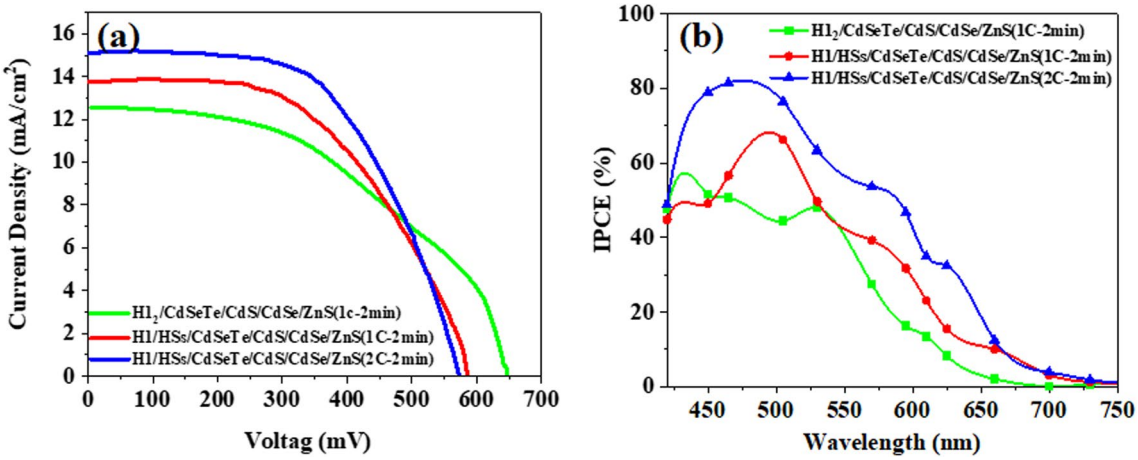

Fig. 8 **a** *J–V* (**b**) and IPCE curves of the fabricated QDSCs with $H1_2$/CdSeTe/CdS/CdSe/ZnS(1c-2 min) and H1/HSs/CdSeTe/CdS(4c)/CdSe(9 min)/ZnS(*N*c-2 min); $N = 1, 2$, photoelectrodes

Table 2 Photovoltaic parameters of the QDSCs with $H1_2$/CdSeTe/CdS/CdSe(9 min)/ZnS(1c-2 min) and H1/HSs/CdSeTe/CdS/CdSe/ZnS(*N*c-2 min), $N = 1, 2$, photoelectrodes

Photoanode	J_{sc} (mA/cm^2)	V_{oc} (mV)	FF	η (%)
$H1_2$/CdSeTe/CdS(4c)/CdSe(9 min)/ZnS(1c-2 min)	12.55	647	0.47	3.80
H1/HSs/CdSeTe/CdS(4c)/CdSe(9 min)/ZnS(1c-2 min)	13.75	586	0.53	4.25
H1/HSs/CdSeTe/CdS(4c)/CdSe(9 min)/ZnS(2c-2 min)	15.1	575	0.57	4.95

electrolyte interface. Besides, the 3 cycles of ZnS deposition did not work and the corresponding QDSC was disconnected due to the strong ZnS potential barrier in front of the necessary hole transfer in QDs/electrolyte interface. The incident photon to current conversion efficiency (IPCE) analysis was also performed for the mentioned fabricated QDSCs. As shown in Fig. 8b, the spectra are spread in the wavelength range of 400–700 nm. This is related to the light absorption by different CdSeTe, CdS, CdSe-sensitizing QDs layers. Meanwhile, the lowest intensity among the IPCE spectra belongs to the reference cell with $H1_2$/CdSeTe/CdS/CdSe(9 min)/ZnS(1c-2 min) photoelectrode. The IPCE curves are improved for the HSs included QDSCs and maximum IPCE values are related to the pioneer cell with H1/HSs/CdSeTe/CdS/CdSe/ZnS(2c-2 min) photoanode. This is in correspondence with the results of J–V curves and demonstrates the effectiveness of HSs application and optimization of the passivation layer.

4 Conclusion

In this work the effect of CdSe QDs layer, light scattering TiO_2 HSs layer and passivizing film on the PV performance of CdSeTe/CdS-sensitized QDSCs were investigated. Several structural, optical an elemental analysis were performed specially concentrated on multi-layer photoelectrodes. The result demonstrated that allocation of CdSe co-sensitizing QDs film through 9 min of CBD process could create an enhance about 30% in PCE. This was attributed to the effective and extra light absorption by optimized CdSe QDs layer and possible electron/hole transport inside the cells. The TiO_2 HSs with sizes around 550 nm were also synthesized and utilized as the over-deposited light scattering layer on the surface of mesoporous TiO_2 NC_S scaffold. This modification could also led to 12% enhancement in the PCE of QDSC with TiO_2 NC_S/HSs/CdSeTe/CdS(9 min)/ZnS photo electrode. Finally a thick ZnS passivizing final over layer was applied and showed another 30% increase in PV performance. It was shown that the best QDSC demonstrated a 68% enhancement in power conversion efficiency compared to that of the CdSe and HSs-free reference cell.

Author contributions All authors contributed to the study conception and design. Material preparation, data collection and analysis were performed by NS, SHA, and MM. The first draft of the manuscript was written by Dr. MM and all authors commented on previous versions of the manuscript. All authors read and approved the final manuscript.

References

1. N. Piven, A.S. Susha, M. Doblinger, A.L. Rogach, J. Phys. Chem. C **112**, 15253–15259 (2008)
2. R. Ross, A. Nozik, J. Appl. Phys. **53**, 3813–3818 (1982)
3. T.K. Nideep, M. Ramya, M. Kailasnath, The influence of ZnS buffer layer on the size dependent efficiency of CdTe quantum dot sensitized solar cell. J. Super Lattice Microstruct. **130**, 175–181 (2019)
4. H.K. Jun, M.A. Careem, A.K. Arof, Quantum dot-sensitized solar cells perspective and recent developments: a review of Cd chalcogenide quantum dots as sensitizers. J. Renew. Sustain. Energy Rev. **22**, 148–167 (2013)
5. P.V. Kamat, Quantum dot solar cells. Semiconductor nanocrystals as light harvesters. J. Phys. Chem. C **112**, 18737–18753 (2008)
6. M. Marandi, E. Rahmani, F.A. Farahani, Optimization of the photoanode of CdS quantum dot-sensitized solar cells using light-scattering TiO_2 hollow spheres. J. Electron. Mater **46**, 6769–6783 (2017)
7. M. Kouhnavard, S. Ikeda, N.A. Ludin, N.B. Ahmad Khairudin, B.V. Ghaffari, M.A. Mat-Teridi, M.A. Ibrahim, S. Sepeai, K. Sopian, A review of semiconductor materials assensitizers for quantum dot-sensitized solar cells. J. Renew. Sustain. Energy Rev. **37**, 397–407 (2014)
8. R.H. Sven, M. Shalom, A. Zaban, Quantum-dot-sensitized solar cells. J. ChemPhysChem **11**, 2290–2304 (2010)
9. M. Gratzel, Photoelectrochemical cells. Nature **414**, 338–334 (2001)
10. Ch. Cai et al., Synthesis of $AgInS_2$ quantum dots with tunable photoluminescence for sensitized solar cells. J. Power Sources **341**, 11–18 (2017)
11. Ru. Zhou et al., Tailoring band structure of ternary CdS_xSe_{1-x} quantum dots for highly efficient sensitized solar cells. Sol. Energy Mater. Sol. Cells **155**, 20–29 (2016)
12. N.J.L.K. Davis et al., Multiple-exciton generation in lead selenide nanorod solar cells with external quantum efficiencies exceeding 120%. Nat. Commun. **6**, 8259 (2015)
13. G. Nair, L.Y. Chang, S.M. Geyer, M.G. Bawendi, Perspective on the prospects of a carrier multiplication nanocrystal solar cell. J. Nano Lett. 2145–2151 (2011)
14. S. Kumara, M. Nehrab, A. Deepc, D. Kediab, N. Dilbaghia, K.H. Kimd, Quantum-sized nanomaterials for solar cell applications. J. Renew. Sustain. Energy Rev. **73**, 821–839 (2017)
15. X. Du, X. He, L. Zhao, H. Chen, W. Li, W. Fang, W. Zhang, J. Wang, H. Chen, TiO_2 hierarchical porous film constructed by ultrastable foams as photoanode for quantum dot-sensitized solar cells. J. Power Sources **332**, 1–7 (2016)
16. D. Wu, X. Shi, H. Dong, F. Zhu, K. Jiang, D. Xu, X. Ai, J. Zhang, The effect of photoanode structure on the performances of quantum-dot-sensitized solar cells: a case study of the anatase TiO_2 nanocrystals and polydisperse mesoporous spheres hybrid photoanodes. J. Mater. Chem. A **2**, 16276–16284 (2014)
17. J. Tian, Q. Zhang, E. Uchaker, Z. Liang, R. Gao, X. Qu, S. Zhang, G. Cao, Constructing ZnO nanorod array photoelectrodes for highly efficient quantum dot sensitized solar cells. J. Mater. Chem. A **1**, 6770–6775 (2013)
18. J. Jie, Z. Zheng-Ji, Z. Wen-Hui, W. Xin, CdS and PbS quantum dots co sensitizedTiO_2 nano rod arrays with improved performance for solar cells application. J. Mater. Sci. Semicond. Process **16**, 435–440 (2013)
19. M. Marandi, F.S. Mirahmadi, Aqueous synthesis of CdTe–CdS core shell nanocrystals and effect of shellformation process on the efficiency of quantum dot sensitized solar cells. J. Sol. Energy **188**, 35–44 (2019)
20. S. Lee et al., High performance of TiO_2/CdS quantum dot sensitized solar cells with a Cu–ZnS passivation layer. New J. Chem. **41**, 1914–1917 (2017)
21. L. Wonjoo, L. Jungwoo, K.M. Sun, P.K. Taehee, Y. Whikun, H. Sung-Hwan, Effect of single-walled carbon nanotube in PbS/TiO_2 quantum dots-sensitized solar cells. J. Mater. Sci. Eng. **156**, 48 (2009)
22. M. Marandi, S. Bayat, Facile fabrication of hyper-branched TiO_2 hollow spheres for high efficiency dye-sensitized solar cells. J. Solar Energy **174**, 888–896 (2018)
23. W. Zhang, X. Zeng, H. Wang, R. Fang, Y. Xu, Y. Zhang, W. Chen, High-yield synthesis of "oriented attachment" TiO_2 nanorods as superior building blocks of photoanodes in quantum dot sensitized solar cells. J. Chen. RSC Adv. **6**, 33713–33722 (2016)
24. Q. Shen, J. Xue, J. Liu, X. Liu, H. Jia, B. Xu, Enhancing efficiency of CdS/TiO_2 nanorod arrays solar cell through improving the hydrophilicity of TiO_2 nanorodsurface. J. Sol. Energy Mater. Sol. Cells **136**, 206 (2015)
25. M. Marandi, S. Bayat, M. NaeimiSaniSabet, Hydrothermal growth of a composite TiO_2 hollow spheres/TiO_2 nanorods powder and its application in high performance dye sensitized solar cells. J. Elechem. **11**, 023 (2018)
26. Z. Zhengji, Y. Shengjie, F. Junqi, H. Zeliang, Z. Wenhui, D. Zuliang, $CuInS_2$ quantum dot-sensitized TiO_2 nanorod array photoelecrodes: synthesis and performance optimization. J. Nano Scale Res. Lett. **7**, 652 (2012)
27. T. Auttasit, L. Ming-Way, W. Gou-Jen, Ag_2Se quantum-dot sensitized solar cells for full solar spectrum light harvesting. J. Power Sources **196**, 6603–6608 (2011)
28. Z. Chen, W. Peng, K. Zhang, J. Zhang, X. Yang, Y. Numata, L. Han, Band alignment by ternary crystalline potential-tuning interlayer for efficient electron injection in quantum dot-sensitized solar cells. J. Mater. Chem. A **2**, 7004–7014 (2014)
29. S. Chand, A. Dahshan, N. Thakur, V. Sharma, P. Sharma, Alloyed $Ag_2Se_xS_{1-x}$ quantum dots with red to NIR shift: the bandgap tuning with dopant content for energy harvesting applications. J. Infrared **105**, 103162 (2019)
30. D. Liua, J. Liua, J. Liua, S. Liua, C. Wanga, Z. Gea, X. Haoa, N. Duc, H. Xia, The photovoltaic performance of CdS/CdSe quantum dots co-sensitized solar cells based on zinc titanium mixed metal oxides. J. Phys. Low-Dimens. Syst. Nanostruct. **115**, 113669 (2020)
31. P. Ma, Y. Fang, H. Cheng, Y. Wang, X. Zhou, S. Fang, Y. Lin, NH_2-rich silica nanoparticle as a universal additive in electrolytes for high-efficiency quasi-solid-state dye-sensitized solar cells and quantum dot sensitized solar cells. J. Electrochim. Acta **262**, 197 (2018)
32. P. Naresh Kumar, A. Kolay, S. Krishna Kumar, P.K. Patra, A.N. Aphale, A. Kumar Srivastava, M. Deepa, The counter electrode impact on quantum dot solar cell efficiencies. (2016)
33. G. Jiang, Z. Pan, Z. Ren, J. Du, C. Yang, W. Wang, X. Zhong, Poly(vinyl pyrrolidone) a superior and general additive in polysulfide electrolyte for high efficiency quantum dot sensitized solar cells. J. Mater. Chem. A C6TA04027F (2016)
34. U. Ahmed, M. Alizadeh, N. Abd Rahim, S. Shahabuddin, M.S. Ahmed, A.K. Pandey, A comprehensive review on counter electrodes for dye sensitized solar cells: a special focus on Pt-TCO free counter electrodes. J. Sol. Energy **174**, 1097–1125 (2018)
35. Z. Tachan, M. Shalom, I. Hod, S. Rühle, S. Tirosh, A. Zaban, PbS as a highly catalytic counter electrode for polysulfide-based quantum dot solar cells. J. Phys. Chem. **115**, 6162–6166 (2011)
36. J. Yu, W. Wang, Z. Pan, J. Du, Z. Ren, W. Xuea, X. Zhong, Quantum dot sensitized solar cells with efficiency over 12% based on tetraethyl orthosilicate additive in polysulfide electrolyte. J. Mater. Chem. **A5**, 14124 (2017)

37. K.E. Roelofs, T.P. Brennan, J.C. Dominguez, C.D. Bailie, G.Y. Margulis, E.T. Hoke, M.D. McGehee, S.F. Bent, Effect of Al_2O_3 recombination barrier layers deposited by atomic layer deposition in solid-state CdS quantum dot-sensitized solar cells. J. Phys. Chem. C **117**, 5584–5592 (2013)
38. L. Mu, C. Liu, J. Jia, X. Zhou, Y. Lin, Dual post-treatment: a strategy towards high efficiency quantum dot sensitized solar cells. J. Mater. Chem. A **1**, 8353–8357 (2013)
39. Y. Lin, Yu. Lin, Y. Meng, Y. Wang, CdS quantum dots sensitized ZnO spheres via ZnS overlayer to improve efficiency for quantum dots sensitized solar cells. J. Ceram. Int. **40**, 8157–8163 (2014)
40. M. Marandi, M. Nazari, Application of TiO_2 hollow spheres and ZnS/SiO_2 double-passivaiting layers in the photoanode of the CdS/CdSe QDs sensitized solar cells for the efficiency enhancement. J. Solar Energy. **216**, 48–60 (2021)
41. M. Abdul Basit, N. Ali, Superior ZnS deposition for augmenting the photostability and photovoltaic performance of PbS quantum-dot sensitized solar cells. Chem. Phys. Lett. **731**, 136572 (2019)
42. M. Marandi, S. HosseinAbadi, Aqueous synthesis of colloidal $CdSe_xTe_{1-x}$–CdS core-shell nanocrystals and effect of shell formation parameters on the efficiency of corresponding quantum dot sensitized solar cells. J. Solar Energy. **209**, 387–399 (2020)
43. R.E. Bailey, S.M. Nie, Alloyed semiconductor quantum dots: tuning the optical properties without changing the particle size. J. Am. Chem. Soc. **125**(23), 7100–7106 (2003)
44. J. Yang, J. Wang, K. Zhao, T. Izuishi, Y. Li, Q. Shen, X. Zhong, CdSeTe/CdS type-I core/shell quantum dot sensitized solar cells with efficiency over 9%. J. Phys. Chem. **119**, 28800–28808 (2015)
45. P.V. Kamat, K. Tvrdy, D.R. Baker, J.G. Radich, Beyond photovoltaics: semiconductor nanoarchitectures for liquid-junction solar cells. J. Chem. Rev **110**, 6664–6688 (2010)
46. A.J. Nozik, M.C. Beard, J.M. Luther, M. Law, R.J. Ellingson, J.C. Johnson, Semiconductor quantum dots and quantum dot arrays and applications of multiple exciton generation to third generation photovoltaic solar cells. J. Chem. Rev **11**, 6873–6890 (2010)
47. M. Marandi, N. Torabi, F. Ahangarani Farahani, Facile fabrication of well-performing CdS/CdSe quantum dot sensitized solar cells through a fast and effective formation of the CdSe nanocrystalline layer. J. Solar Energy **207**, 32–39 (2020)
48. C.V. Gopi, V.M. Venkata-Haritha, M. Kim, S.-K., H.-J. Kim, Improved photovoltaic performance and stability of quantum dot sensitized solar cells using Mn–ZnSe shell structure with enhanced light absorption and recombination control. J. Nanoscale 7: 12552–12563 (2015).
49. M.S. Fuente, R.S. Sanchez, V. Gonzalez-Pedro, P.P. Boix, S.G. Mhaisalkar, M.E. Rincon, Effect of organic and inorganic passivation in138 quantum-dot-sensitized solar cells. J. Phys. Chem. Lett. **4**, 1519–1525 (2013)
50. E. Robert, Bailey, S. Nie, Alloyed semiconductor quantum dots: tuning the optical properties without changing the particle size. J. Am. Chem. Soc. **125**(23), 7100–7106 (2003)
51. H. Wei, G. Wan, Y. Luo, D. Li Qingbo Meng, Investigation on interfacial charge transfer process in $CdSe_xTe_{1-x}$ alloyed quantum dot sensitized solar cells. J. Electr. Acta **173**, 156–163 (2015)
52. R. Herrera, R. Velázquez, A. Meda, P. Delgado, T. Guízar, Taboad, P. Luis, NIR-emitting alloyed CdTeSe QDs and organic dye assemblies: a nontoxic, stable, and efficient FRET system. J. Nanomater. **4**, E231 (2018)
53. J. Albero, J.N. Clifford, E. Palomares, Quantum dot based molecular solar cells. J. Coord. Chem. Rev **263**, 53–64 (2014)
54. L.E. Brus, Electron—electron and electron-hole interactions in small semiconductor crystallites: the size dependence of the lowest excited electronic state. J. Chem. Phys. **80**, 4403–4409 (1984)
55. Zh. Pan, K. Zhao, J. Wang, H. Zhang, Y. Feng, X. Zhong, Near infrared absorption of $CdSe_xTe_{1-x}$ alloyed quantum dot sensitized solar cells with more than 6% efficiency and high stability. J. Am. Chem. Soc. Nano **6**, 5215–5222 (2013)
56. D. Esparza, E. Del La Rosa, Enhancement of efficiency in quantum dot sensitized solar cells based on CdS/CdSe/CdSeTe heterostructure by improving the light absorbtion in the VIS-NIR region. J. Electrochimica Acta **247**, 899–909 (2017)
57. Z. Pan, I. Mora-Sero, Q. Shen, H. Zhang, Y. Li, K. Zhao et al., High-efficiency "green" quantum dot solar cells. J. Am. Chem. Soc. **136**, 9203–9210 (2014)
58. X. Zhang, J. Liu, E.M.J. Johansson, Efficient charge-carrier extraction from Ag_2S quantum dots prepared by the SILAR method for utilization of multiple exciton generation. Nanoscale **7**, 1454–1462 (2014)
59. S.-H. Weia, S.B. Zhang, A. Zunger, First-principles calculation of band offsets, optical bowings, and defects in CdS, CdSe, CdTe, and their alloys. J. Aip **87**, 1304 (2000)
60. M. Ostadebrahimi, H. Dehghani, $ZnS/CdSe_{0.2}S_{0.8}$/ZnSSe heterostructure as a novel and efficient quantum dot sensitized solar cells. J. Appl. Surf. Sci. **545**, 148958 (2021)
61. G. Liu, Z.-B. Ling, Y. Wang, H. Zhao, Near-infrared $CdSe_xTe_{1-x}$/CdS "giant" quantum dots for efficient photoelectrochemical hydrogen generation. J. Hydrog. Energy **43**, 22064–22074 (2018)
62. S. Majumder, P.K. Baviskar, B.R. Sankapal, Light-induced electrochemical performance of 3D-CdS nanonetwork: effect of annealing. Electrochim. Acta. **222**, 100–107 (2016)
63. P. Scherrer, Bestimmung der Grosse und der Inneren Struktur von Kolloidteilchen Mittels Rontgenstrahlen. Nachrichten von der Gesellschaft der Wissenschaften, Mathematisch-Physikalische **2**, 98–100 (1918)
64. A.J. Longford, Wilson Scherrer after sixty years: a survey and some new results in the determination of crystallite size. J. Appl. Crystallogr. **11**, 102–113 (1978)